CHEMISTRY OF MATERIALS

Article

pubs.acs.org/cm

Intertwining Roles of Silver Ions, Surfactants, and Reducing Agents in Gold Nanorod Overgrowth: Pathway Switch between Silver Underpotential Deposition and Gold–Silver Codeposition

Qingfeng Zhang,[†] Hao Jing,[†] Guangfang Grace Li,[†] Ye Lin,[‡] Douglas A. Blom,[§] and Hui Wang*[,†]

[†]Department of Chemistry and Biochemistry, [‡]Department of Chemical Engineering, and [§]USC Nanocenter, University of South Carolina, Columbia, South Carolina 29208, United States

Supporting Information

ABSTRACT: The past two decades have witnessed great success achieved in the geometry-controlled synthesis of metallic nanoparticles using the seed-mediated nanocrystal growth method. Detailed mechanistic understanding of the synergy among multiple key structure-directing agents in the nanocrystal growth solutions, however, has long been lagging behind the development and optimization of the synthetic protocols. Here we investigate the foreign ion- and surfactant-coguided overgrowth of single-crystalline Au nanorods as a model system to elucidate the intertwining roles of Ag^+ foreign ions, surface-capping surfactants, and reducing agents that underpin the intriguing structural evolution of Au nanocrystals. The geometry-controlled nanorod overgrowth involves two distinct underlying pathways, Ag underpotential deposition and Au–Ag electroless codeposition, which are interswitchable upon maneuvering the interplay of the Ag^+ ions, surfactants, and reducing agents. The pathway switch governs the geometric and compositional evolution of nanorods during their overgrowth, allowing the cylindrical Au nanorods to selectively transform into a series of anisotropic nanostructures with interesting geometric, compositional, and plasmonic characteristics. The insights gained from this work shed light on the mechanistic complexity of geometry-controlled nanocrystal growth and may guide the development of new synthetic approaches to metallic nanostructures with increasing architectural complexity, further enhancing our capabilities of fine-tuning the optical, electronic, and catalytic properties of the nanoparticles.

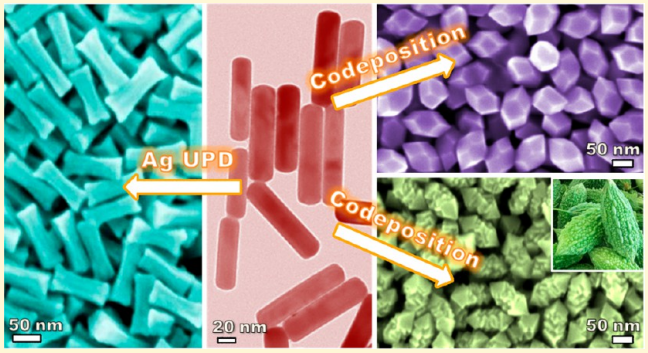

INTRODUCTION

Recent advances in colloidal nanoparticle synthesis have greatly enhanced our capabilities of fine-tuning the optical, electronic, and catalytic properties of metallic nanoparticles through deliberate control over the particle shapes and compositions.[1−5]

Seed-mediated nanocrystal growth, in particular, provides a highly robust and versatile approach to the precise geometry control of metallic nanoparticles under mild conditions.[5−13] The seed-mediated structural evolution of nanocrystals is synergistically guided by a set of interplaying geometric, kinetic, and thermodynamic factors such as the crystallinity of seeds,[5,10,14] the supersaturation of crystal growth units,[15] the thermodynamic stabilities of various crystallographic facets,[16] and the selective passivation of nanocrystal surfaces.[10] An extensive library of anisotropic nanoparticle geometries, such as nanorods,[6,17−21] nanoprisms,[22] and a series of low-index and high-index faceting nanopolyhedrons,[12,13,16,23−31] have been experimentally realized through kinetically controlled seed-mediated nanocrystal growth processes with the aid of structure-directing surfactants and foreign ion additives. These synthetic protocols, however, have been developed and optimized in a largely empirical fashion, while detailed nanocrystal growth mechanisms often remained ambiguous until recently a coherent mechanistic understanding of shape-controlled growth of Au nanocrystals started to emerge in the literature.[32]

The geometric evolution of Au nanocrystals during seed-mediated growth is essentially governed by two primary pathways: kinetic control of nanocrystal growth and selective passivation of nanoparticle surfaces.[10,32] Under the kinetic control pathway, fast nanocrystal growth facilitates the formation of kinetically favored high-index faceting nanocrystals, such as {221}-faceting nanotrisoctahedrons,[10,33−35] whereas slower nanocrystal growth generally results in thermodynamically more stable, low-index faceting nanoparticles such as nanocubes enclosed by {100} facets and nanooctahedrons enclosed by {111} facets.[10,32] In contrast, selective passivation of nanoparticle surfaces by capping surfactants or foreign ions offers an alternative pathway that leads to the formation of exotic geometries bound entirely by the passivated facets.[10,27,31] While these two pathways appear divergent at first glance, there is a strong synergy between them. The key components in the

Received: January 29, 2016
Revised: March 14, 2016
Published: March 25, 2016

DOI: 10.1021/acs.chemmater.6b00389
Chem. Mater. 2016, 28, 2728−2741

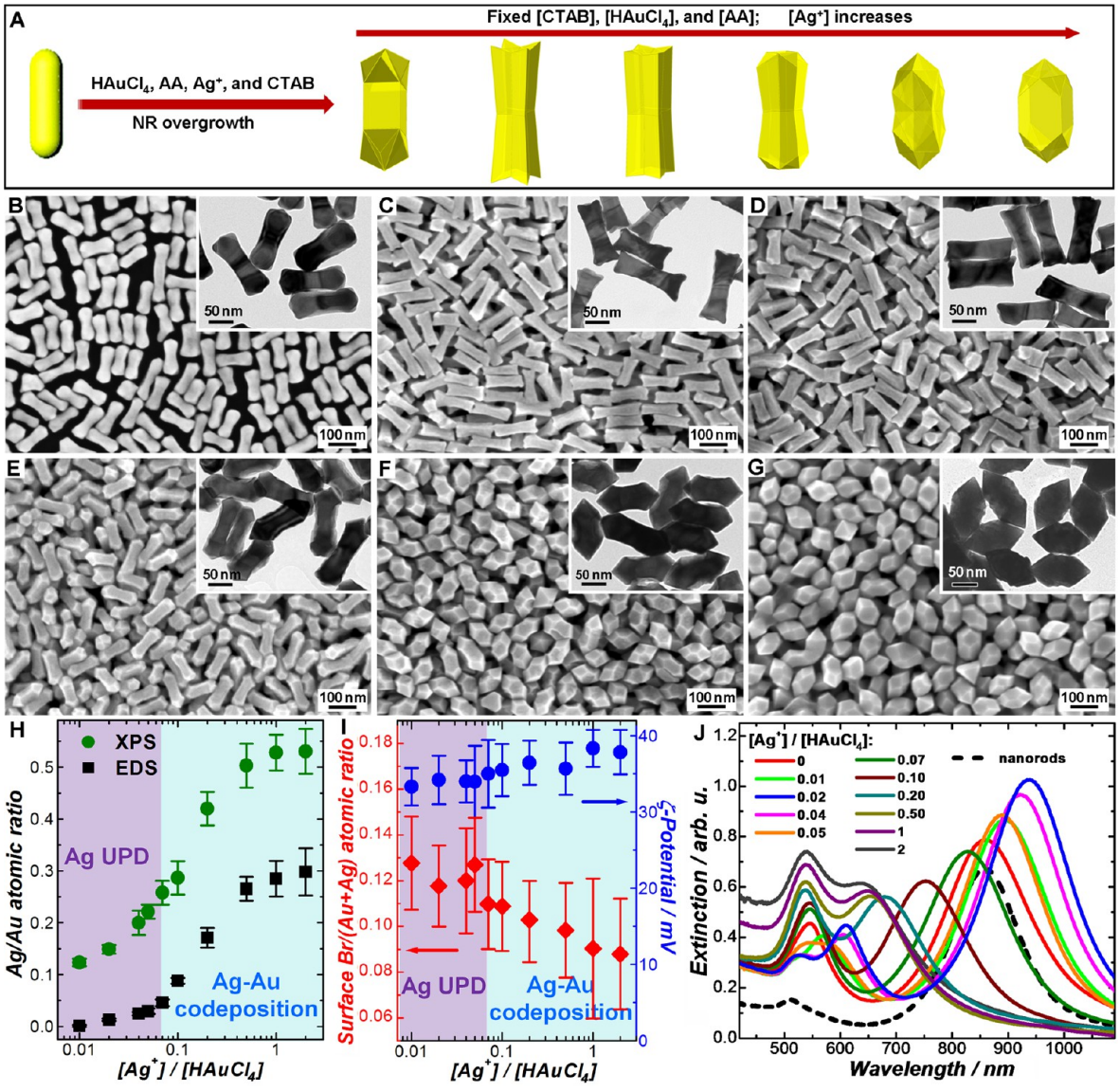

Figure 1. (A) Schematic illustration of geometric evolution during NR overgrowth in the presence of fixed concentrations of $HAuCl_4$, AA, and CTAB but varying concentrations of Ag^+ ions. SEM and TEM (inset) images of the overgrown NRs obtained at various $[Ag^+]/[HAuCl_4]$ ratios of (B) 0, (C) 0.02, (D) 0.05, (E) 0.07, (F) 0.50, and (G) 2.0. The concentrations of CTAB, $HAuCl_4$, and AA were 20 mM, 200 μM, and 10 mM, respectively. (H) Ag/Au atomic ratios of the overgrown NRs obtained at various $[Ag^+]/[HAuCl_4]$ ratios. The bulk and surface Ag/Au atomic ratios were quantified by EDS and XPS, respectively. (I) Surface atomic ratios of Br/(Au + Ag) quantified by XPS and apparent ζ-potentials of the overgrown NRs obtained at various $[Ag^+]/[HAuCl_4]$ ratios. The error bars in panels H and I represent the standard deviations of three samples fabricated under identical conditions. (J) Optical extinction spectra of the overgrown NRs obtained at various $[Ag^+]/[HAuCl_4]$ ratios as labeled in the figure.

nanocrystal growth solutions, including the surfactants, the foreign ions, and the reducing agents, all play multiple intertwining roles in guiding the structural evolution of nanocrystals and may modulate the interswitch between multiple nanocrystal growth pathways. A particularly interesting phenomenon manifesting such mechanistic complexity is the underpotential deposition (UPD) of up to a monolayer of foreign metal adatoms on the Au nanoparticle surfaces during foreign ion-guided Au nanocrystal growth.[10,27,31,32,36−40] The UPD adlayer not only selectively passivates various Au facets, but also fine-regulates the overall nanocrystal growth kinetics, allowing Au nanocrystals to evolve into a variety of low-index and high-index faceting geometries in a highly controllable manner. Under appropriate conditions, the foreign metal ions may also be coreduced with Au through seed-mediated electroless codeposition processes to form heterostructured or homogeneously alloyed multimetallic nanoparticles with further increased architectural and compositional complexity.[41−46]

Among various anisotropic Au nanostructures, single-crystalline cylindrical Au nanorods (NRs) have been of particular interests owing to their intriguing aspect ratio-dependent plasmonic properties.[6,7,19,20] The most popular protocols for NR synthesis involve seed-mediated growth coguided by a foreign metal ion, Ag^+, and halide-containing cationic surfactants, such as cetyltrimethylammonium bromide (CTAB), in the presence of ascorbic acid (AA), which serves as a mild reducing agent.[6,17−19] While the aspect ratios of Au NRs can be fine-tuned by simply varying the concentration of Ag^+ ions in the growth solution, the exact roles that Ag^+ ions play in the symmetry-breaking of the isotropic seeds and the

DOI: 10.1021/acs.chemmater.6b00389
Chem. Mater. 2016, 28, 2728−2741

subsequent anisotropic NR growth still remain elusive and controversial.[36,47−50] In striking contrast to the excellent control over NR aspect ratios, limited success has been achieved so far in the precise facet control of NRs using the seed-mediated growth method. The surface curvature and local facets of Au NRs may change drastically upon even slight variation of the ingredients in the NR growth solutions, and quantitative assignments of the crystallographic facets exposed on the highly curved NR surfaces have long been under intense debate.[17,51−56]

A unique way to further fine-tailor the crystallographic facets and expand the aspect ratio tuning range of Au NRs involves the shape-controlled overgrowth of preformed cylindrical NRs.[57−69] In the absence of foreign metal ions, cylindrical Au NRs may selectively undergo tip overgrowth, isotropic overgrowth, and anisotropic overgrowth to evolve into peanut-shaped NRs, cuboidal NRs, and truncated nano-octahedrons, respectively, depending on the concentrations of CTAB in the overgrowth solutions.[60] Recently, we further demonstrated that more rigorous control of Au NR facets with atomic level precision could be achieved using cuprous (Cu^+) foreign ions and halide-containing surfactants as unique pairs of surface capping competitors to maneuver the facet evolution during NR overgrowth.[68,69] In comparison to Cu^+ ions, Ag^+ ions have been more widely used in combination with various surfactants to guide the morphology-controlled overgrowth of Au NRs. A large variety of NR-derived anisotropic geometries, such as nanodumbbells, starfruit-shaped NRs, dogbone-like NRs, concave nanocuboids, and arrow-headed NRs, have been obtained through Ag^+- and CTAB-coguided NR overgrowth processes.[57,58,61,63−67] However, it still remains a significant challenge to obtain a unified picture that rigorously interprets the interplay of multiple evolutionary pathways involved in the NR overgrowth processes. In this work, we endeavor to pinpoint the intertwining roles of Ag^+ ions, surfactants, and reducing agents in directing the structural and compositional evolution during NR overgrowth with a primary focus on the effects of two interswitchable pathways, specifically Ag UPD and Au−Ag codeposition, on the geometries and compositions of the overgrown NRs.

RESULTS AND DISCUSSION

Single-crystalline cylindrical Au NRs were prepared through a seed-mediated growth process in the presence of Ag^+ ions and CTAB/oleate binary surfactant mixtures[70] and were subsequently employed as the seeds for the postfabrication NR overgrowth. As shown by the scanning electron microscopy (SEM) and transmission electron microscopy (TEM) images in Figure S1 in the Supporting Information, the as-fabricated Au NRs were highly uniform and monodisperse with diameters of 21 ± 3 nm and lengths of 105 ± 5 nm. It was previously reported that Ag existed as either a UPD layer of Ag adatoms or arguably as a AgBr adlayer on the NR surfaces, which was further capped with a positively charged, self-assembled bilayer of CTAB.[17] While the bulk composition of the NRs was dominated by Au as shown by the energy dispersive spectroscopy (EDS) results, both Ag and Br signals were well-resolved by X-ray photoelectron spectroscopy (XPS), clearly verifying the presence of both Ag and CTAB on the NR surfaces (Figure S2 in the Supporting Information). Starting with these preformed cylindrical Au NRs, we performed detailed investigations on the structural and compositional transformations upon NR overgrowth as a function of three variables: Ag^+ ions, capping surfactants, and reducing agents.

Effects of Ag^+ Ions. We symmetrically varied the concentration of Ag^+ ions while keeping $HAuCl_4$ (Au precursor), CTAB, and AA at fixed concentrations of 200 μM, 20 mM, and 10 mM, respectively. As schematically illustrated in Figure 1, panel A, the cylindrical Au NRs transformed into a series of interesting NR-derived anisotropic geometries as the Ag^+ concentration in the overgrowth solution progressively increased. In the absence of Ag^+ ions, the Au NRs transformed into elongated trisoctahedral nanoparticles (ETOH NPs) (Figure 1B), which is in line with our previous observations.[69] Detailed electron microscopy characterizations revealed that each ETOH NP was enclosed by four {110} lateral side facets and 24 high-index {221} facets at the two ends.[69] The formation of the kinetically favored, high-index faceting ETOH NPs was a direct consequence of fast NR overgrowth at sufficiently high $[AA]/[HAuCl_4]$ ratios ($[AA]/[HAuCl_4] = 50$ in this case). Overgrowth of quasi-spherical Au nanoparticles under similar conditions resulted in the formation of high-index faceting nanotrisoctahedrons each of which was enclosed by 24 {221} facets.[34] In the presence of Ag^+ ions, strikingly different geometric transformations were observed upon NR overgrowth. As shown in Figure 1, panel C, surface concavity was developed on the NR surfaces at relatively low $[Ag^+]/[HAuCl_4]$ ratios below 0.02, forming dog bone-like nanorods (DBLNRs) with eight sharp tips. Upon further increase of the $[Ag^+]/[HAuCl_4]$ ratio, however, the surface indentation and tip sharpness of the DBLNRs both gradually decreased, while the transverse dimensions of the overgrown NRs progressively increased (Figure 1D,E), eventually leading to the formation of arrow-headed NRs (AHNRs) with two sharp tips, each of which was enclosed by four thermodynamically stable {111} facets (Figure 1F,G). The evolution of the transverse and longitudinal dimensions of the overgrown NRs obtained at different $[Ag^+]/[HAuCl_4]$ ratios is shown in Figure S3 in the Supporting Information. Apparently, Ag^+ ions played crucial roles in directing the morphological evolution of NRs under the current NR overgrowth conditions.

To further elucidate the exact roles of Ag^+ ions, we used EDS and XPS to characterize the bulk and surface compositions of the overgrown NRs, respectively. Both EDS and XPS results (Figure S4 in the Supporting Information) showed the absence of Ag on the ETOH NPs, verifying that the formation of ETOH NPs was purely a CTAB-mediated, kinetically controlled process without the involvement of Ag^+ foreign ions. At low $[Ag^+]/[HAuCl_4]$ ratios below 0.07, the bulk compositions of the overgrowth NRs were essentially dominated by Au with Ag signals almost undetectable by EDS. However, strong Ag signals were clearly resolved in XPS, and the surface Ag/Au atomic ratios measured by XPS exhibited much higher values than the bulk Ag/Au atomic ratios obtained from EDS (Figure S5 in the Supporting Information). The sample penetration depth of the XPS measurements under the current experimental conditions was calibrated to be ∼1 nm, which roughly corresponded to five atomic layers from the outer surface of the nanoparticles. Therefore, a Ag/Au atomic ratio of ∼0.25 corresponded to a saturated monolayer coverage of Ag UPD adatoms on the Au nanoparticle surfaces. As the $[Ag^+]/[HAuCl_4]$ ratio increased from 0.01 to 0.07, the surface Ag/Au atomic ratios (measured by XPS) progressively increased from ∼0.12 to ∼0.26, while the bulk Ag/Au atomic ratios (measured by EDS) remained below

DOI: 10.1021/acs.chemmater.6b00389
Chem. Mater. 2016, 28, 2728−2741

0.03 (Figure 1H), well reflecting the transition of a submonolayer to a fully saturated monolayer of Ag UPD adatoms on the surfaces of the overgrown NRs. Both the EDS and XPS results strongly indicated that the transformation of cylindrical Au NRs into the DBLNRs was governed by a Ag UPD-dominated overgrowth pathway.

As the $[Ag^+]/[HAuCl_4]$ ratio further increased to above 0.07, Ag^+ and $HAuCl_4$ started to be coreduced by AA to form Au−Ag alloy shells surrounding the Au NR cores, resulting in the formation of Au−Ag bimetallic AHNRs. EDS and XPS results shown in Figure S6 in the Supporting Information clearly verified the Au NR-core and Au−Ag alloy-shell heterostructure of the AHNRs. Much higher Ag content was detected by both EDS and XPS on the AHNRs than on the DBLNRs, and a sharp increase of both the bulk and surface Ag/Au atomic ratios was observed over a narrow $[Ag^+]/[HAuCl_4]$ window (Figure 1H). In the high $[Ag^+]/[HAuCl_4]$ ratio regime, the NR overgrowth was dominated by Au−Ag electroless codeposition, a pathway fundamentally different from the Ag UPD. The Ag atoms in the AHNRs were intermixed with Au atoms far beyond the surface atomic layer to form alloy structures. We also performed angle-dependent XPS measurements to further contrast the compositional difference between DBLNRs and AHNRs. The maximal probe penetration depth (~1 nm) was achieved at normal incidence, while the probe penetration depth decreased as the detector was shifted away from normal incidence with respect to the sample surfaces (Figure S7A in the Supporting Information). The surface Ag/Au atomic ratios of DBLNRs progressively increased as the probe penetration depth decreased, whereas the AHNRs exhibited surface Ag/Au atomic ratios that were almost independent of the probe penetration depth (Figure S7B in the Supporting Information). Meanwhile, both the DBLNRs and AHNRs exhibited surface Br/Au atomic ratios that progressively increased with decrease in probe penetration depth, verifying that the CTAB surfactant molecules existed on the surfaces of the overgrown NRs. The angle-dependent XPS results provided strong evidence that Ag UPD adatoms were present on the surface of DBLNRs, while an AHNR was composed of a Au NR core surrounded by a Ag−Au alloy shell. Therefore, DBLNRs can be considered as a product of Ag UPD-guided NR overgrowth, while the transformation of Au NRs into AHNRs was dominated by Ag−Au codeposition. More interestingly, the pathway inter-switch between the Ag UPD and Ag−Au codeposition can be modulated by simply tuning the $[Ag^+]/[HAuCl_4]$ ratios with a threshold value around 0.07 for the pathway switch (Figure 1H).

Under all the experimental conditions mentioned above ($[Ag^+]/[HAuCl_4] < 2$), no precipitation of AgBr was observed during the NR overgrowth. However, when the $[Ag^+]/[HAuCl_4]$ ratio further increased to 4, insoluble AgBr started to form, which resulted in mixtures of AHNRs and irregularly shaped, micron-sized AgBr (see Figure S8 in the Supporting Information). To avoid the complication due to AgBr precipitation, the structural evolution during NR overgrowth at $[Ag^+]/[HAuCl_4]$ ratio higher than 2 was not further explored.

We qualitatively assessed the surface packing density of CTAB on the overgrown NRs by plotting surface atomic ratio of Br/(Au+Ag) (quantified by XPS) as a function of the $[Ag^+]/[HAuCl_4]$ ratio in the overgrowth solutions. As shown in Figure 1, panel I, the CTAB packing densities on the DBLNRs appeared higher than those on AHNRs. The XPS results also showed that the Br/(Au+Ag) ratio was independent of the Ag/(Au+Ag) ratio of the DBLNRs, suggesting that the surface of a DBLNR was capping with a CTAB surfactant layer rather than a AgBr adlayer. However, XPS was incapable of further distinguishing the Ag(0) from Ag(I) species because of the spectral overlap between Ag(0) and Ag(I). To gain further insights into the nature of surface-deposited Ag, we correlated the XPS results with the nanoparticle surface charges characterized by ζ-potential measurements. In our ζ-potential measurements, a commercial ζ-potentiometer was used to measure the free mobility and effective hydrodynamic sizes of the colloidal nanoparticles, which were then converted into apparent ζ-potentials using simple theoretical formulas approximating each particle as a hard sphere homogeneously coated with a charged thin layer. Although more accurate determination of ζ-potentials requires the incorporation of additional empirical or semiempirical parameters, such as the geometric anisotropy and heterogeneous distribution of adsorbates on various facets,[71] into the theoretical formulas, the apparent ζ-potentials reported here allowed us to qualitatively compare the relative surface charges of the nanoparticles of various NR-like geometries. Interestingly, the apparent ζ-potentials of the DBLNRs remained essentially unchanged regardless of the variation of the $[Ag^+]/[HAuCl_4]$ ratios (Figure 1I). Both the XPS and ζ-potential results suggested that the surface packing density of CTAB on the overgrown DBLNRs was independent of the $[Ag^+]/[HAuCl_4]$ ratios in the NR overgrowth solutions. When the Au−Ag codeposition dominated the NR overgrowth, however, the apparent ζ-potentials started to increase with the $[Ag^+]/[HAuCl_4]$ ratios despite the decrease in the surface packing density of CTAB, suggesting that additional Ag^+ ions may be physicorbed on the surfaces of AHNRs when the Ag^+ concentration is sufficiently high. More quantitative assessment of Ag(0) and Ag(I) species on the nanoparticle surfaces, however, requires detailed investigations using advanced structural characterization techniques such as synchrotron Ag K-edge extended X-ray absorption fine-structure (EXAFS)[40] and small-angle neutron scattering (SANS)[72] measurements.

Complementary to the SEM and TEM measurements, the structural transformations of NRs upon their overgrowth can also be monitored using optical extinction spectroscopy owing to the geometry-dependent plasmonic characteristics of the nanoaprticles (Figure 1J). The cylindrical Au NRs displayed a strong longitudinal plasmon resonance at ~860 nm and a much weaker transverse plasmon resonance at ~510 nm, respectively. In the low $[Ag^+]/[HAuCl_4]$ ratio regime where Ag UPD dominated the NR overgrowth, both the longitudinal and transverse plasmon resonances red-shifted and became stronger as the Au NRs evolved into DBLNRs largely due to the formation of surface concavity. We also found that the transverse plasmon mode of DBLNRs split into two peaks, which is a spectral signature of NRs with surface indentations.[63,68] As the degree of surface indentation of the DBLNRs decreased, both the longitudinal and transverse plasmon peaks gradually blue-shifted accompanied by decrease in peak intensities. When the Au−Ag codepostion started to dominate the NR overgrowth at higher $[Ag^+]/[HAuCl_4]$ ratios, corner truncation of the DBLNRs led to further blue-shift and weakening of the longitudinal plasmon peak, while the transverse plasmon peak remained robust at essentially fixed wavelengths. The transverse plasmon peak became much stronger than the longitudinal plasmon peak when the NRs

DOI: 10.1021/acs.chemmater.6b00389
Chem. Mater. 2016, 28, 2728−2741

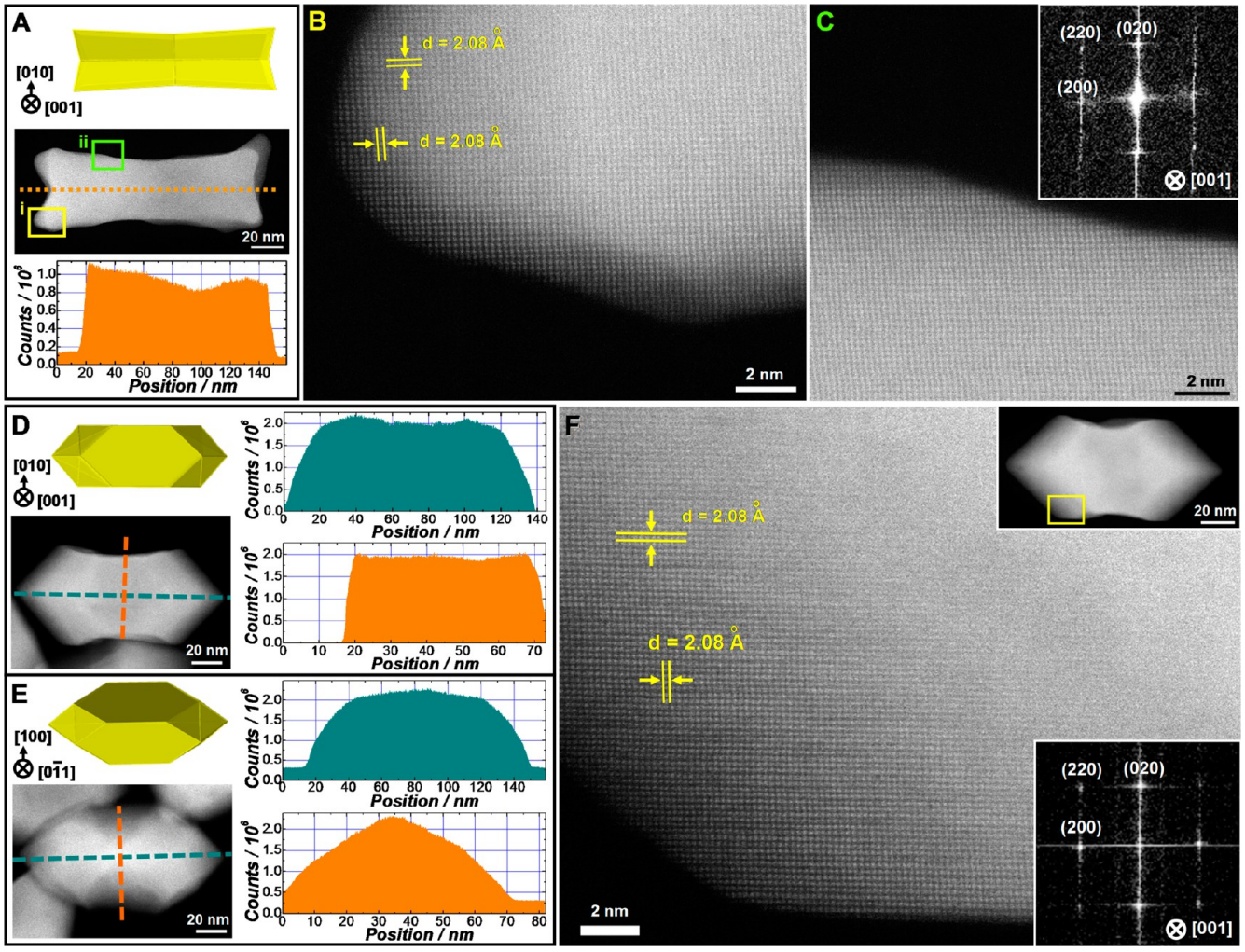

Figure 2. (A) HAADF-STEM image and the corresponding geometric model of an individual Au DBLNR projected along the [001] zone axis, together with the intensity profiles along the line labeled in panel A. High-resolution HAADF-STEM images of (B) region i and (C) region ii labeled in panel A. The inset in panel C is the fast Fourier transform (FFT) pattern of the image. HAADF-STEM images and the corresponding geometric models of individual AHNRs projected along (D) [001] and (E) [0$\bar{1}$1] zone axes. The intensity profiles along the lines labeled in each panel were also shown. (F) High-resolution HAADF-STEM images of a portion of an individual AHNR. The HAADF-STEM image of the entire AHNR and the specific region in the high-resolution image are shown in the upright inset. The bottom right inset is the corresponding FFT pattern of the high-resolution HAADF-STEM image.

eventually evolved into AHNRs at sufficiently high $[Ag^+]/[HAuCl_4]$ ratios.

We used high-angle annular dark-field scanning transmission electron microscopy (HAADF-STEM) to further characterize the atomic-level structures of the DBLNRs and AHNRs (Figure 2). The relative orientation of each DBLNR or AHNR with respect to the electron beam was verified by the crystalline lattices in the high-resolution HAADF-STEM images and the fast-Fourier transform (FFT) patterns of the images. Figure 2, panel A shows the geometric model and HAADF-STEM image of a single-crystalline DBLNR projected along the [001] zone axis. The surface indentation of the DBLNR was well reflected by the line-scan image intensity profiles (the image intensity was roughly proportional to the thickness of the specimen). Figure 2, panels B and C show the high-resolution HAADF-STEM images of the regions i and ii labeled in Figure 2, panel A, respectively. Because of the small lattice mismatch between Au and Ag (<0.2%), only one set of face centered cubic lattices was resolved in the high resolution HAADF-STEM image. The concave surfaces of a DBLNR were essentially enclosed by various types of high-index facets whose Miller indices were determined by the local surface curvatures. Figure 2, panels D and E show the HAADF-STEM images and geometric models of individual AHNRs projected along the [001] and [0$\bar{1}$1] zone axis, respectively. The 3D geometries of the AHNRs were qualitatively confirmed by the orientation-dependent line-scan intensity profiles. The (100) crystalline lattices were clearly resolved in the high resolution HAADF-STEM image when an AHNR was projected along the [001] zone axis (Figure 2F). The lateral side facets of an AHNR were dominated by low-index {100} facets, while the longitudinal tips of an AHNR were enclosed by low-index {111} facets. Under the Ag UPD pathway, the side facets were selectively passivated by the UPD adlayers, while the growth of corners was facilitated, resulting in the formation of high-index faceting DBLNRs with concave surfaces and increased longitudinal dimensions. In contrast, Ag−Au codeposition preferentially occurred on the lateral side facets to form thermodynamically more stable, low-index faceting AHNRs with significantly increased transverse dimensions.

DOI: 10.1021/acs.chemmater.6b00389
Chem. Mater. 2016, 28, 2728−2741

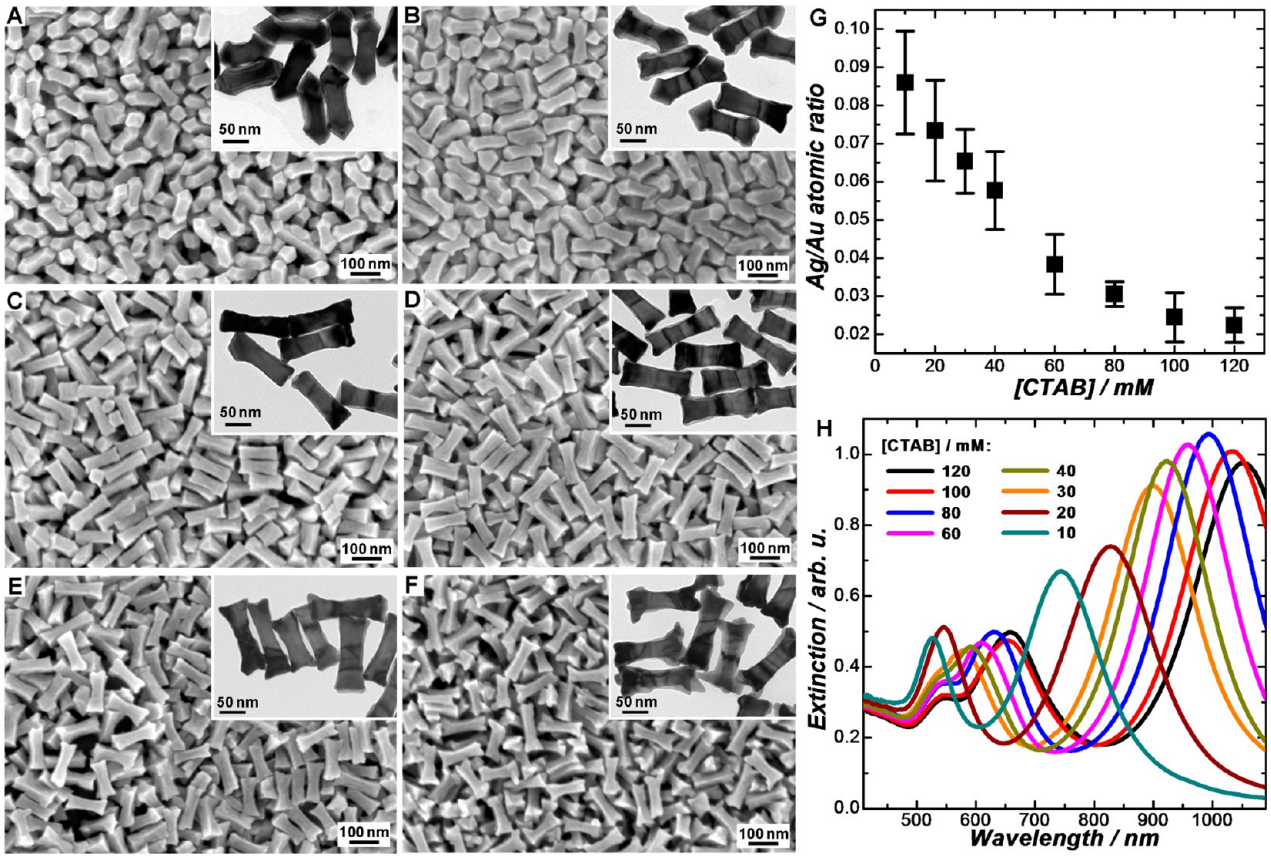

Figure 3. SEM and TEM (inset) images of overgrown NRs obtained in (A) 10 mM, (B) 20 mM, (C) 30 mM, (D) 60 mM, (E) 80 mM, and (F) 120 mM CTAB. The Ag^+, AA, and $HAuCl_4$ concentrations were kept at 14 μM, 10 mM, and 200 μM, respectively. (G) Ag/Au atomic ratios (quantified by EDS) of the overgrown NRs obtained at various CTAB concentrations. The error bars represent the standard deviations of three samples fabricated under identical conditions. (H) Optical extinction spectra of the overgrown NRs obtained in various concentrations of CTAB as labeled in the figure.

Effects of Surface Capping Surfactants. The pathway switch between Ag UPD and Au−Ag codeposition could also be maneuvered by varying the concentration of the CTAB surfactants while keeping Ag^+, $HAuCl_4$, and AA at fixed concentrations. Figure 3, panels A−F show the SEM and TEM images of the nanoparticles obtained upon NR overgrowth in the presence of 200 μM $HAuCl_4$, 10 mM AA, 14 μM Ag^+, and various concentrations of CTAB. At relatively low CTAB concentrations (e.g., [CTAB] = 10 mM), AHNRs were obtained. As the concentration of CTAB progressively increased, surface indentation and corner protrusion gradually emerged, eventually leading to the formation of DBLNRs with shape tips and highly indented surfaces at CTAB concentrations above 80 mM. The structural transition from AHNRs to DBLNRs was essentially caused by the pathway switch from Ag−Au codeposition to Ag UPD, which was further verified by EDS (Figure 3G). As the concentration of CTAB increased, both the longitudinal and transverse plasmon resonances progressively red-shifted and became increasingly more intense (Figure 3H), well-reflecting the transition from AHNRs to DBLNRs with increasing degrees of surface indentation. Under the current NR overgrowth conditions, CTAB served as a surface-capping competitor to the Ag^+ foreign ions, providing another key knob for the pathway interswitch. Therefore, it is the ratio of $[Ag^+]/[CTAB]$ rather than the absolute concentrations of Ag^+ and CTAB that modulates the pathway switch between Ag UPD and Ag−Au codeposition.

To gain more detailed insights into the effects of Ag UPD layers on the surface indentation of DBLNRs, we systematically varied the concentration of Ag^+ ions in the NR overgrowth solutions while keeping CTAB at a sufficiently high concentration (150 mM) such that the pathway switch from Ag UPD to Au−Ag codepostion was effectively suppressed. In the presence of 150 mM CTAB, the NR overgrowth was always dominated by the Ag UPD pathway when the $[Ag^+]/[CTAB]$ ratio was varied over a broad range from 0.1−0.75. The degree of surface indentation and the sharpness of the tips of the DBLNRs progressively decreased as the $[Ag^+]/[CTAB]$ ratio increased (Figure 4A−D). While the Ag signals were very low in EDS, the surface Ag/Au atomic ratios were measured to be in the range of 0.2−0.25 by XPS for the DBLNRs with various degrees of surface indentation (Figure 4E), verifying the presence of a Ag UPD adlayer on the nanoparticle surfaces. The capability of tuning the surface indentation and tip sharpness of the DBLNRs, when combined with the fine-control over aspect ratios, enables the tuning of the plasmon resonance frequencies and extinction spectral line-shapes of NRs with greater detail and precision. As shown in Figure 4, panel F, sharper tips and more significant surface indentation gave rise to larger spectral red-shifts of both the transverse and longitudinal plasmon resonances.

To further test the hypothesis that the pathway switch was maneuvered by the competition between Ag^+ ions and capping surfactants, we used benzyldimethylhexadecylammonium chlor-

DOI: 10.1021/acs.chemmater.6b00389
Chem. Mater. 2016, 28, 2728−2741

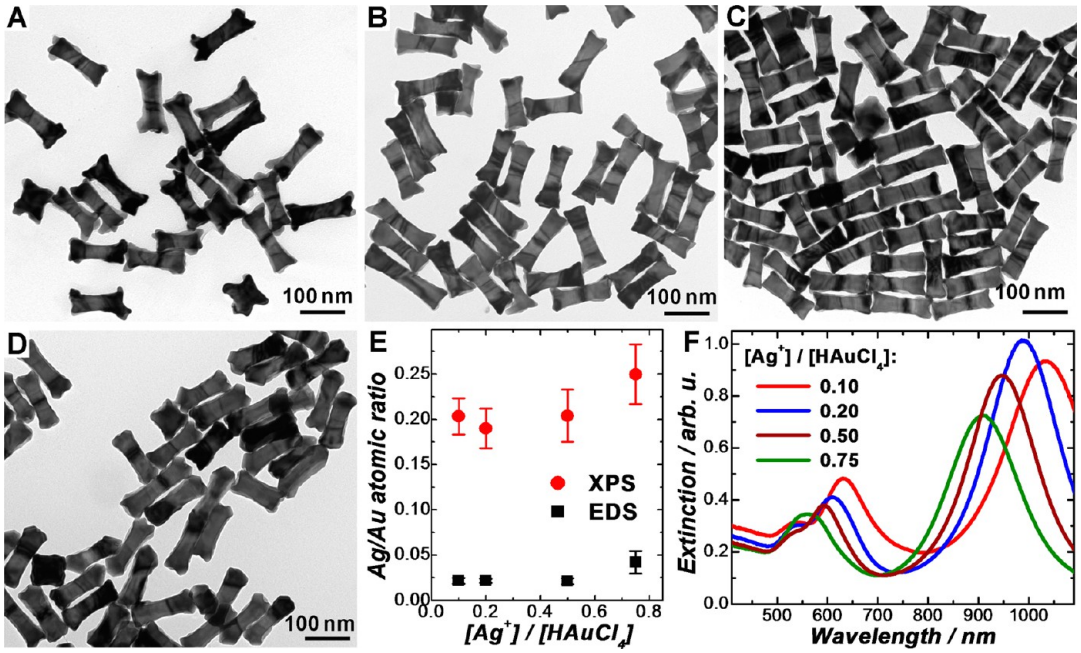

Figure 4. TEM images of overgrown NPs obtained in the presence of 150 mM CTAB at various $[Ag^+]/[HAuCl_4]$ ratios of (A) 0.10, (B) 0.20, (C) 0.50, and (D) 0.75. The concentrations of $HAuCl_4$ and AA were 200 μM and 10 mM, respectively. (E) Ag/Au atomic ratios determined by EDS and XPS for the overgrown NRs obtained at various $[Ag^+]/[HAuCl_4]$ ratios. The error bars represent the standard deviations of three samples fabricated under identical conditions. (F) Optical extinction spectra of the overgrown NRs obtained in the presence of 150 mM CTAB and various $[Ag^+]/[HAuCl_4]$ ratios as labeled in the figure.

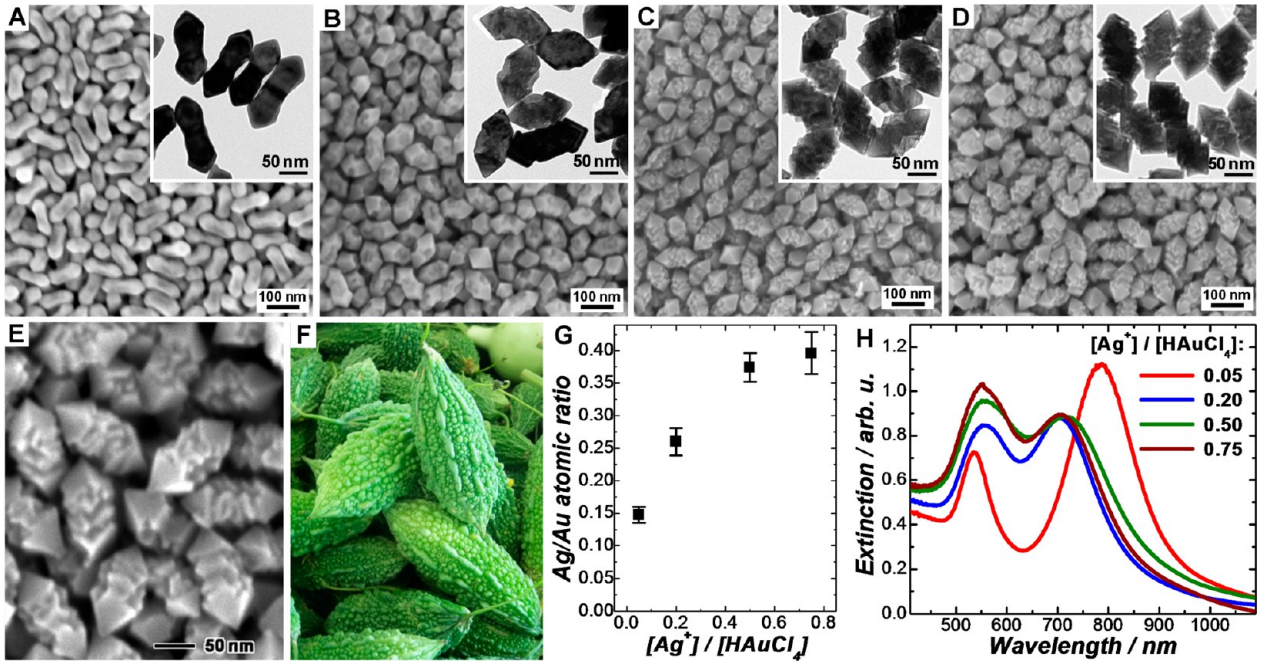

Figure 5. SEM and TEM (inset) images of overgrown NRs obtained in the presence of 30 mM BDAC at various $[Ag^+]/[HAuCl_4]$ ratios of (A) 0.05, (B) 0.20, (C) 0.50, and (D) 0.75. The concentrations of $HAuCl_4$ and AA were fixed at 200 μM and 10 mM, respectively. (E) High-magnification SEM image of Au@Ag–Au MCLNRs obtained at $[Ag^+]/[HAuCl_4]$ ratio of 0.75. (F) Photograph of momordica charantias. (G) Ag/Au atomic ratios, determined by EDS, of NPs obtained at various $[Ag^+]/[HAuCl_4]$ ratios. The error bars represent the standard deviations of three samples fabricated under identical conditions. (H) Optical extinction spectra of NPs obtained through NR overgrowth in the presence of 30 mM BDAC and various $[Ag^+]/[HAuCl_4]$ ratios as labeled in the figure.

ide (BDAC) instead of CTAB as the capping surfactants to guide the NR overgrowth. At a $[Ag^+]/[HAuCl_4]$ ratio of 0.05, AHNRs were obtained in the presence of 30 mM BDAC (Figure 5A), while DBLNRs were obtained in 30 mM CTAB under otherwise identical NR overgrowth conditions (Figure S9 in the Supporting Information). Apparently, the substitution of CTAB with BDAC switched the NR overgrowth pathway from Ag UPD to the Ag–Au codeposition. Such pathway switch could be interpreted as a consequence of the weaker interactions of BDAC than those of CTAB with Au

DOI: 10.1021/acs.chemmater.6b00389
Chem. Mater. 2016, 28, 2728–2741

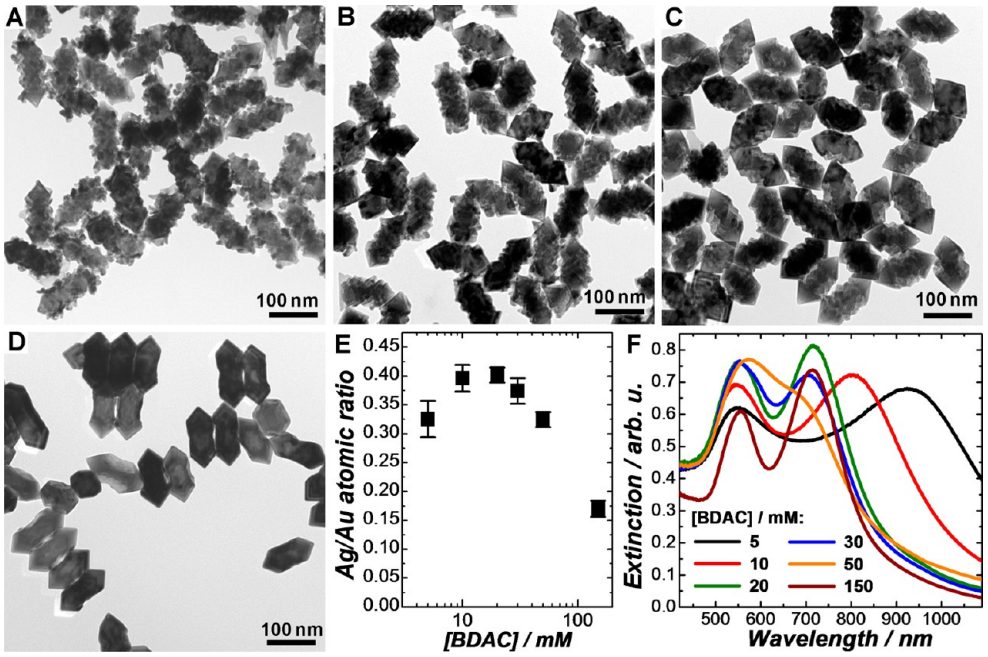

Figure 6. TEM images of overgrown NRs obtained in (A) 5 mM, (B) 10 mM, (C) 50 mM, and (D) 150 mM BDAC. The concentrations of Ag^+, $HAuCl_4$, and AA were fixed at 20 μM, 200 μM, and 10 mM, respectively. (E) Ag/Au atomic ratios, determined by EDS, of NPs obtained at various BDAC concentrations. The error bars represent the standard deviations of three samples fabricated under identical conditions. (F) Optical extinction spectra of the overgrown NRs obtained in the presence of various concentrations of BDAC as labeled in the figure.

surfaces.[10,73] The relative binding affinities of CTAB and BDAC on Au surfaces were further verified by the surfactant exchange between CTAB and BDAC monitored by surface-enhanced Raman spectroscopy (SERS) measurements (Figures S10 and S11 in the Supporting Information). More detailed discussion on the SERS results is included in the Supporting Information. In the presence of 30 mM BDAC, nanoscale roughness started to develop on the lateral side surfaces of the AHNRs as the $[Ag^+]/[HAuCl_4]$ ratio increased, while the {111} facets at the tips were preserved (Figure 5B–D), leading to the formation of a unique structure resembling momordica charantias, inspiring the name momordica charantia-like nanorods (MCLNRs) (Figure 5E,F). The EDS results (Figure S12 in Supporting Information) clearly showed that each MCLNR was composed of a Au NR core and a Ag–Au alloy shell. The Ag/Au atomic ratios obtained from EDS progressively went up to ~0.40 with the increase of the $[Ag^+]/[HAuCl_4]$ ratios, indicating that the transformation of Au NRs into MCLNRs was dominated by Ag–Au electroless codeposition (Figure 5G). As shown in Figure 5, panel H, the structural evolution from AHNRs to MCLNRs caused significant blue-shift and weakening of the longitudinal plasmon resonance largely due to the increased transverse dimensions and Ag content of the particles.

The morphological interconversions between MCLNRs and AHNRs could also be achieved through variation of the BDAC concentration while keeping Ag^+, $HAuCl_4$, and AA at fixed concentrations. As shown in Figure 6, panels A–D, the MCLNRs gradually became less rough on their lateral side surfaces as the concentration of BDAC increased, eventually transforming into AHNRs at sufficiently high BDAC concentrations. The Ag/Au atomic ratios of MCLNRs were significantly higher than those of the AHNRs, though the $[Ag^+]/[HAuCl_4]$ ratio in the NR overgrowth solutions was kept the same (Figure 6E). During the geometric transition from MCLNRs to AHNRs, the longitudinal plasmon resonance progressively blue-shifted, and the peak width significantly decreased as a consequence of decrease in aspect ratios, while the transverse plasmon resonance wavelength remained essentially unchanged (Figure 6F).

Both the cationic amphiphilic chain and the halide anion of the surfactant molecules play crucial roles in guiding the NR structural evolution. The surfactants interact with the nanoparticle surfaces primarily through metal–halide interactions. During surfactant-guided, seed-mediated nanocrystal growth, the presence of additional halide anions may drastically modify the geometries of the resulting Au nanoparticles due to the metal–halide interactions.[74−76] However, we found that the halide anions alone without the surfactants were incapable of controlling the geometry of overgrown NRs. In the presence of the halide-containing cationic surfactants, the Au(III) precursor is reduced to Au(I) by AA, which forms Au(I)–surfactant complexes that are soluble in water.[18] Upon addition of Au NR seeds into the overgrowth solution, a surface-catalyzed electroless plating process occurs, through which Au(I) is further reduced to metallic Au on the surfaces of Au NRs.[18] Without any surfactants, Au(III) was rapidly reduced to metallic Au, while Ag(I) was coreduced to metallic Ag in the presence of KBr or KCl even before the introduction of Au NR seeds, resulting in the formation of highly aggregated Au–Ag bimetallic nanoparticles (Figure S13 in the Supporting Information). To further elucidate the roles of the halide anions in the surfactants, we substituted CTAB with cetyltrimethylammonium chloride (CTAC), a chloride-containing surfactant with exactly the same amphiphilic chain as that of CTAB, to guide the NR overgrowth under otherwise identical experimental conditions. As shown in Figures S14A–C in the Supporting Information, substitution of 20 mM CTAB with 20 mM CTAC resulted in a morphological change from DBLNRs to AHNRs primarily because chloride anions have

DOI: 10.1021/acs.chemmater.6b00389
Chem. Mater. 2016, 28, 2728–2741

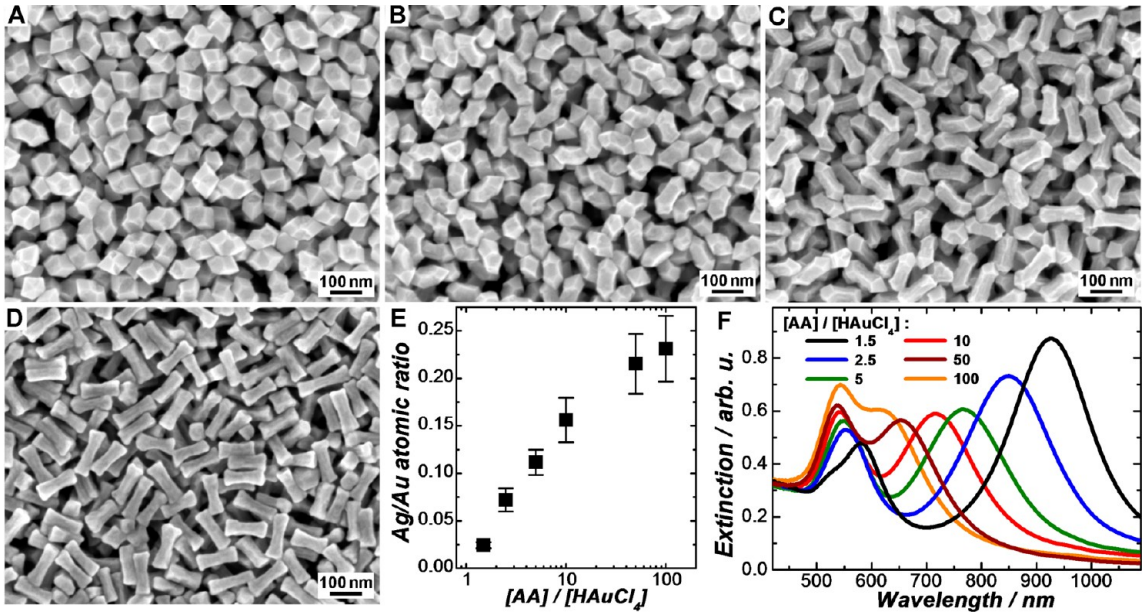

Figure 7. SEM images of overgrown NRs obtained at various $[AA]/[HAuCl_4]$ ratios of (A) 100, (B) 10, (C) 2.5, and (D) 1.5. The concentrations of Ag^+, CTAB, and $HAuCl_4$ were kept at 100 μM, 20 mM, and 200 μM, respectively. (E) Ag/Au atomic ratios (quantified by EDS) of the overgrown NRs obtained at various $[AA]/[HAuCl_4]$ ratios. The error bars represent the standard deviations of three samples fabricated under identical conditions. (F) Optical extinction spectra of the overgrown NRs obtained at various $[AA]/[HAuCl_4]$ ratios as labeled in the figure.

weaker interactions with Au than bromide anions and thus are less efficient to compete with Ag^+ ions. On the other hand, the packing density of the surfactants on the nanoparticle surfaces is intimately tied to the structures of the amphiphilic chains. Although both CTAC and BDAC contain the same anion, the cationic chain of BDAC is bulkier than that of CTAC due to the presence of benzene ring. As a result, substitution of 30 mM BDAC with 30 mM CTAC switched the morphology of the overgrown NRs from MCLNRs to AHNRs (Figures S14D–F in the Supporting Information) possibly due to denser packing of CTAC on the nanoparticle surfaces than that of BDAC.

We analyzed the detailed XPS spectral features of the Au 4f and Ag 3d peaks of the overgrown NRs of various geometries and compositions (Figure S15 in the Supporting Information). The Ag/Au surface atomic ratios labeled in Figure S15A,B were quantified by XPS, and a table listing the positions of Au 4f and Ag 3d peaks was shown in Figure S15C. The XPS spectra of bulk Au and Ag foils were also included for comparison. On the bulk Ag foil, two well separated spin–orbital components were observed at 368.2 eV (Ag $3d_{5/2}$) and 374.2 eV (Ag $3d_{3/2}$), respectively, and weak loss features were also observed to the higher binding energy side of each spin–orbit component for Ag. The loss features, however, became undetectable on the Ag-containing overgrown NR samples due to the change of atomic coordination environment of Ag atoms upon the formation of either a Ag UPD layer or a Ag–Au alloy shell. While the Au 4f peaks only slightly shifted within ±0.1 eV, the Ag 3d peaks exhibited significantly more pronounced spectral down-shifts up to −0.5 eV upon the formation of a Ag UPD layer or a Ag–Au alloy shell, which is in excellent agreement with previously reported XPS results on Ag UPD layer-coated Au nanoparticles[27] and Au–Ag alloy nanoparticles.[77,78]

Effects of Reducing Agents. In addition to the interplay between Ag^+ ions and surfactants, the reducing agents also played a key role in maneuvering pathway interswitch between Ag UPD and Ag–Au codeposition. To further investigate the effects of reducing agents, we fixed the concentrations of CTAB, $AgNO_3$, and $HAuCl_4$ at 20 mM, 100 μM, and 200 μM, respectively, while systematically varying the AA concentrations. At relatively high $[AA]/[HAuCl_4]$ ratios, the preferential codeposition of Ag and Au resulted in the formation of Au@Ag–Au AHNRs (Figure 7A). As the $[AA]/[HAuCl_4]$ ratios gradually decreased, and Ag UPD began to dominate the NR overgrowth process, giving rise to the formation of DBLNRs with truncated corners, which further evolved into DBLNRs with sharper tips and more significant surface indentation (Figures 7B–D). The evolution of Ag/Au atomic ratios (Figure 7E) and optical extinction spectral features (Figure 7F) provided additional evidence on the pathway switch from Ag–Au codeposition to Ag UPD as AA concentration decreased. This strongly indicated that fast NR overgrowth in the presence of high concentrations of AA favored the Au–Ag codeposition. The NR overgrowth was slowed down when decreasing the AA concentrations, which caused the pathway switch from Au–Ag codeposition to Ag UPD.

To better understand the effects of reducing agents, we also used other mild reducing agents, such as hydroquinone (HQ) and 4-(2-hydroxyethyl)-1-piperazineethanesulfonic acid (HEPES), to initiate the NR overgrowth. Because the reducing capabilities of both HQ and HEPES are significantly weaker than those of AA,[79,80] the NR overgrowth became much slower when using HQ and HEPES instead of AA under otherwise identical conditions. By keeping the molar ratio of reducing agents to $HAuCl_4$ fixed at 50, AHNRs were obtained in the presence of AA, whereas the use of HQ and HEPES resulted in the formation of DBLNRs (Figure S16 in Supporting Information). Therefore, the NR overgrowth kinetics controlled by the reducing agents is also a key factor determining the pathway interswitch between Ag UPD and Au–Ag codeposition.

As summarized in the literature, the geometric evolution of Au nanocrystals during seed-mediated growth is primarily governed by two pathways: kinetic control and selective surface passivation.[32] In absence of foreign metal ions, high-index

DOI: 10.1021/acs.chemmater.6b00389
Chem. Mater. 2016, 28, 2728–2741

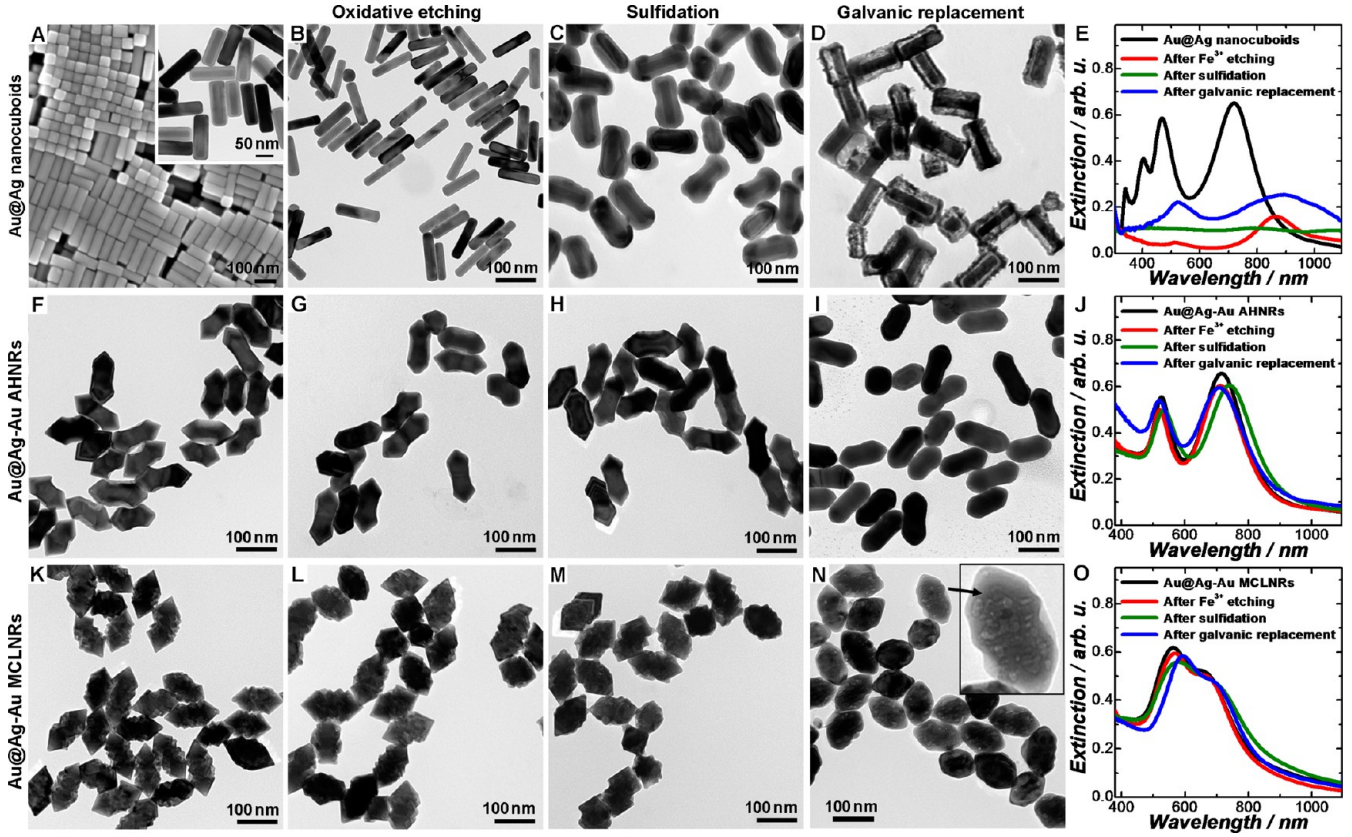

Figure 8. (A) SEM and TEM (inset) images of Au@Ag core−shell NCBs. TEM images of Au@Ag core−shell NCBs after (B) oxidative etching by Fe^{3+}, (C) sulfidation with Na_2S, and (D) galvanic replacement with $HAuCl_4$. (E) Optical extinction spectra of the NPs shown in panels A−D. TEM images of (F) AHNRs, (G) AHNRs after oxidative etching by Fe^{3+}, (H) AHNRs after sulfidation with Na_2S, and (I) AHNRs after galvanic replacement with $HAuCl_4$. (J) Optical extinction spectra of the NPs shown in panels F−I. TEM images of (K) MCLNRs, (L) MCLNRs after oxidative etching by Fe^{3+}, (M) MCLNRs after sulfidation with Na_2S, and (N) MCLNRs after galvanic replacement with $HAuCl_4$. The inset of panel N shows a high-magnification TEM of one particle indicated by an arrow. (O) Optical extinction spectra of the NPs shown in panels K−N.

faceting nanoparticles were typically the major products of fast nanocrystal growth processes, while slow growth kinetics favored the formation of thermodynamically stable low-index faceting nanoparticles. In the presence of Ag^+ foreign ions, the surfaces of Au nanoparticle were selectively passivated by Ag UPD adlayers, guiding the transformation of Au nanocrystals into a variety of high-index faceting geometries.[10,27] Higher Ag^+ concentrations resulted in the formation of facets with higher-order Miller indices.[27] In striking contrast to these previous observations, we found that slow NR overgrowth allowed the cylindrical Au NRs to transform into high-index faceting DBLNRs, whereas fast NR overgrowth led to the formation of low-index faceting AHNRs. Apparently, the geometric evolution of NRs observed in this work should not be simply interpreted as the consequence of either a kinetically controlled or a surface passivation-dominated nanocrystal growth process. It was essentially the pathway interswitch between Ag UPD and Au−Ag codeposition that underpinned the intriguing structural evolution of cylindrical Au NRs into various Au−Ag bimetallic nanoparticle geometries.

Structural Stability of Ag−Au Bimetallic AHNRs and MCLNRs. Ag nanostructures exhibit highly desired plasmonic properties for widespread applications; however, they are chemically much less stable than the other noble metal counterparts such as Au, Pt, and Pd nanopartricles. An effective way to stabilize the Ag nanoparticles while retaining their key plasmonic characteristics is to homogeneously alloy elemental Ag with elemental Au in nanocrystals. As previously demonstrated in various Ag−Au alloy nanoparticles, the interdiffusion of Ag atoms into Au matrix through alloying greatly enhanced the stability of Ag elements, and higher oxidation potentials were required to trigger the oxidation of Ag when it was alloyed.[65,66,81] While nanostructures similar to the AHNRs can be fabricated through NR overgrowth under various conditions,[37,65,66,82] there has long been lack of consensus on the exact compositions of the AHNRs. An AHNR was initially identified to be a Au NR core coated with either a Ag UPD adlayer[37] or a monometallic Ag nanoshell.[82] However, more recent studies revealed that each AHNR was essentially a heteronanostructure composed of a Au-core and a Ag−Au alloy shell,[65,66] which well interpreted the structural robustness of the AHNRs against chemical etching.[65,66] As demonstrated in this work, the Au−Ag codeposition-controlled NR overgrowth provided a unique way to electrolessly deposit Ag−Au alloy shells on Au NR cores.

We systematically compared the structural changes of three representative Ag−Au bimetallic heteronanostructures, Ag@Ag core−shell nanocuboids (NCBs), Au@Au−Ag core−shell AHNRs, and Au@Au−Ag core−shell MCLNRs, upon oxidative etching by Fe^{3+}, sulfidation with Na_2S, and galvanic replacement with $HAuCl_4$ (Figure 8). The monometallic Ag shells were completely etched upon exposure of the NCBs to Fe^{3+}, whereas both the AHNRs and MCLNRs were extremely robust against oxidative etching (Figure 8B,G,L). The relative

DOI: 10.1021/acs.chemmater.6b00389
Chem. Mater. 2016, 28, 2728−2741

resistivities of various nanoparticles toward oxidative etching were further evaluated by electrochemical measurements. A strong anodic peak was observed at ~0.56 V versus SCE in the cyclic voltamogram (CV) of Au@Ag core−shell NCBs, which was attributed to the oxidation of the metallic Ag shells. In contrast, much weaker anodic peaks were observed for both AHNRs and MCLNRs at significantly more positive potentials, indicating that alloying of Ag with Au shifted the Ag oxidation potential to much higher values and the oxidation of Ag also became kinetically inhibited (Figure S17 in the Supporting Information). The structural robustness of Ag−Au alloys was further confirmed by the sulfidation reactions with Na_2S. While the Au@Ag core−shell NCBs completely transformed into Au@Ag_2S core−shell nanoparticles upon sulfidation (Figure 8C and Figure S18 in the Supporting Information), no significant morphological or compositional change was observed on AHNRs and MCLNRs (Figure 8H,M). Upon the exposure of the NCBs to $HAuCl_4$, fast galvanic replacement reactions occurred, which gave rise to the formation of Au@Ag−Au yolk−shell particles with interior cavities[83,84] (Figure 8D). For AHNRs, the sharpness of the tips and edges decreased, while all the facets were well-preserved because the undercoordinated corner and edge atoms were less stable than the surface atoms on the low-index facets of the AHNRs (Figure 8I). The MCLNRs appeared to be more reactive than AHNRs as evident by the formation of nanoscale porosity upon galvanic replacement (Figure 8N) mostly likely due to the fact that the Ag/Au atomic ratios of MCLNRs were higher than those of AHNRs and BDAC provided less effective surface protection in comparison to CTAB.

All the above-mentioned structural transformation processes could be tracked by optical extinction spectroscopy. As shown in Figure 8, panel E, Au@Ag core−shell NCBs exhibited four distinct plasmon resonance bands, which could be assigned to the longitudinal dipole, transverse dipole, transverse octupole, and even high-order multipole resonances, respectively.[85−88] Upon complete etching of the Ag shells with $Fe(NO_3)_3$, only the spectral features of pure Au NR cores were preserved. Interestingly, significant plasmon damping was observed upon the sulfidation of the Ag shells into Ag_2S shells due to the spectral overlap between interband transitions of Ag_2S with the plasmon resonances of Au.[89] The galvanic replacement of NCBs gave rise to significant red-shift and broadening of both the transverse and longitudinal plasmon band upon the formation of the yolk−shell structures, which was in line with previous observations.[83,84] For AHNRs and MCLNRs, no obvious spectral changes were observed due to the structural robustness of these two structures against the oxidative etching, sulfidation, and galvanic replacement treatments (Figure 8J,O).

CONCLUSIONS

This work highlights the intertwining roles of Ag^+ foreign ions, surface-capping surfactants, and reducing agents that underpin the intriguing geometric and compositional evolution of single-crystallline Au NRs upon their overgrowth. The interplay of Ag^+ ions, surfactants, and reducing agents modulates the switch between two underlying NR overgrowth pathways, Ag UPD and Au−Ag electroless codepostion. The interswitch between the two pathways allows cylindrical Au NRs to selectively evolve into a variety of NR-derived anisotropic geometries with interesting structural, compositional, and plasmonic characteristics. The selective surface passivation of Au NRs by Ag UPD adlayers leads to the transformation of cylindrical Au NRs into DBLNRs with concave surfaces enclosed by high-index facets, whereas the Au−Ag codeposition-dominated NR overgrowth processes result in the formation of low-index faceting AHNRs and MCLNRs with Au−Ag alloy shell structures. The homogeneous alloying of Ag with Au in the AHNRs and MCLNRs greatly enhances the stability of the Ag elements in the particles, which makes the AHNRs and MCLNRs remarkably more resistive to oxidative etching, sulfidation, and galvanic replacement than their heterostructured Au−Ag core−shell counterparts. The new insights gained from this work provide important information that may guide the rational design and development of new synthetic approaches to architecturally more sophisticated metallic nanostructures, further enhancing our capabilities to fine-tune the optical, electronic, and catalytic properties of metallic nanoparticles through more deliberate and precise control over the particle geometries and compositions.

EXPERIMENTAL SECTION

Nanorod Overgrowth. Single-crystalline cylindrical Au NRs were prepared following a previously published protocol[70] with minor modifications (see details in the Supporting Information). The NR overgrowth was conducted in the presence of Ag^+, $HAuCl_4$, CTAB, and AA at 30 °C under ambient air. The NR overgrowth solution was prepared by sequentially adding H_2O, $HAuCl_4$, $AgNO_3$, and AA into a CTAB solution. After the solution was gently mixed for 30 s, the overgrowth of NRs was initiated by the introduction of 100 μL of the preformed cylindrical Au NRs (in 0.1 M CTAB). The reaction solution was gently mixed for 30 s immediately after the addition of Au NRs and then left undisturbed at 30 °C for 1 h. The obtained nanoparticles were then washed with H_2O twice through centrifugation/redispersion cycles and finally redispersed in 200 μL of 20 mM CTAB. To investigate the effects of Ag^+, CTAB, and AA, the overall concentrations of Ag^+, CTAB, and AA in the NR overgrowth solutions were systematically varied, while the total volume of the nanorod overgrowth solutions was always fixed at 5.0 mL. BDAC and CTAC were also used as an alternative surfactant instead of CTAB to compare the effects of different surfactants on the NR overgrowth. The effects of reducing agents were investigated by varying the concentration of AA in the overgrowth solutions or using other mild reducing agents such as HQ and HEPES.

Characterizations. The TEM images were obtained using a Hitachi H-8000 transmission electron microscope operated at an accelerating voltage of 200 kV. All samples for TEM measurements were dispersed in water and drop-dried on 300 mesh Formvar/carbon-coated Cu grids. SEM and EDS measurements were performed using a Zeiss Ultraplus thermal field emission scanning electron microscope. The samples for SEM and EDS measurements were dispersed in water and drop-dried on silicon wafers. The atomic level structures of the nanoparticles were resolved by aberration-corrected HAADF-STEM using a JEOL 2100F 200 kV FEG-STEM/TEM microscopy equipped with a CEOS CS corrector on the illumination system. The samples for HAADF-STEM measurements were dispersed in water and drop-dried on 400 mesh Cu grids with ultrathin carbon support film (Electron Microscopy Science Inc.). The optical extinction spectra of the nanoparticles were measured on aqueous colloidal suspensions at room temperature using a Beckman Coulter Du 640 spectrophotometer. ζ-Potentials of colloidal nanoparticles were measured at room temperature using ZETASIZER nanoseries (Nano-ZS, Malvern). The samples for ζ−potential measurements were all freshly prepared, centrifuged, and redispersed in 10 mM CTAB (pH ~ 7.8). XPS measurements were carried out using a Krato AXIS Ultra DLD XPS system equipped with a monochromatic Al Kα source. The samples for XPS measurements were all freshly prepared and dried in vacuum before being loaded into the XPS chambers. SERS spectra were obtained on a Bayspec *Nomadic* confocal Raman microscopy built on an Olympus BX51 microscope equipped with a 785 nm continuous wave diode laser. CV measurements were performed in 0.1 M KNO_3

DOI: 10.1021/acs.chemmater.6b00389
Chem. Mater. 2016, 28, 2728−2741

electrolyte solution at room temperature. More details of SERS and CV measurements are presented in the Supporting Information.

■ ASSOCIATED CONTENT

Supporting Information

The Supporting Information is available free of charge on the ACS Publications website at DOI: 10.1021/acs.chemmater.6b00389.

Additional experimental details, more detailed discussion of the SERS results, and additional figures including SEM images, TEM images, optical extinction spectra, EDS, XPS, CV, and SERS results as noted in the text (PDF)

■ AUTHOR INFORMATION

Corresponding Author

*E-mail: wang344@mailbox.sc.edu. Phone: 1-803-777-2203. Fax: 1-803-777-9521.

Notes

The authors declare no competing financial interest.

■ ACKNOWLEDGMENTS

H.W. acknowledges the support by a National Science Foundation CAREER Award (NSF DMR-1253231), an ASPIRE-I Track-I Award from the University of South Carolina Office of Vice President for Research, and the University of South Carolina Startup Funds. Q.Z. was partially supported by a SPARC Graduate Research Grant from the Office of the Vice President for Research at the University of South Carolina. The authors thank the University of South Carolina Electron Microscopy Center and W.M. Keck Open Laboratory for instrument use and technical assistance.

■ REFERENCES

(1) Burda, C.; Chen, X. B.; Narayanan, R.; El-Sayed, M. A. Chemistry and Properties of Nanocrystals of Different Shapes. *Chem. Rev.* **2005**, *105*, 1025−1102.

(2) Jain, P. K.; Huang, X. H.; El-Sayed, I. H.; El-Sayed, M. A. Noble Metals on the Nanoscale: Optical and Photothermal Properties and Some Applications in Imaging, Sensing, Biology, and Medicine. *Acc. Chem. Res.* **2008**, *41*, 1578−1586.

(3) Tao, A. R.; Habas, S.; Yang, P. D. Shape Control of Colloidal Metal Nanocrystals. *Small* **2008**, *4*, 310−325.

(4) Grzelczak, M.; Perez-Juste, J.; Mulvaney, P.; Liz-Marzan, L. M. Shape Control in Gold Nanoparticle Synthesis. *Chem. Soc. Rev.* **2008**, *37*, 1783−1791.

(5) Xia, Y. N.; Xiong, Y. J.; Lim, B.; Skrabalak, S. E. Shape-Controlled Synthesis of Metal Nanocrystals: Simple Chemistry Meets Complex Physics? *Angew. Chem., Int. Ed.* **2009**, *48*, 60−103.

(6) Murphy, C. J.; Sau, T. K.; Gole, A. M.; Orendorff, C. J.; Gao, J. X.; Gou, L.; Hunyadi, S. E.; Li, T. Anisotropic Metal Nanoparticles: Synthesis, Assembly, and Optical Applications. *J. Phys. Chem. B* **2005**, *109*, 13857−13870.

(7) Perez-Juste, J.; Pastoriza-Santos, I.; Liz-Marzan, L. M.; Mulvaney, P. Gold Nanorods: Synthesis, Characterization and Applications. *Coord. Chem. Rev.* **2005**, *249*, 1870−1901.

(8) Jones, M. R.; Osberg, K. D.; Macfarlane, R. J.; Langille, M. R.; Mirkin, C. A. Templated Techniques for the Synthesis and Assembly of Plasmonic Nanostructures. *Chem. Rev.* **2011**, *111*, 3736−3827.

(9) Sau, T. K.; Rogach, A. L. Nonspherical Noble Metal Nanoparticles: Colloid-Chemical Synthesis and Morphology Control. *Adv. Mater.* **2010**, *22*, 1781−1804.

(10) Langille, M. R.; Personick, M. L.; Zhang, J.; Mirkin, C. A. Defining Rules for the Shape Evolution of Gold Nanoparticles. *J. Am. Chem. Soc.* **2012**, *134*, 14542−14554.

(11) Sau, T. K.; Murphy, C. J. Seeded High Yield Synthesis of Short Au Nanorods in Aqueous Solution. *Langmuir* **2004**, *20*, 6414−6420.

(12) Wang, Y. S.; Sentosun, K.; Li, A.; Coronado-Puchau, M.; Sánchez-Iglesias, A.; Li, S. Z.; Su, X. D.; Bals, S.; Liz-Marzán, L. M. Engineering Structural Diversity in Gold Nanocrystals by Ligand-Mediated Interface Control. *Chem. Mater.* **2015**, *27*, 8032−8040.

(13) Tsao, Y. C.; Rej, S.; Chiu, C. Y.; Huang, M. H. Aqueous Phase Synthesis of Au-Ag Core-Shell Nanocrystals with Tunable Shapes and Their Optical and Catalytic Properties. *J. Am. Chem. Soc.* **2014**, *136*, 396−404.

(14) O'Brien, M. N.; Jones, M. R.; Brown, K. A.; Mirkin, C. A. Universal Noble Metal Nanoparticle Seeds Realized Through Iterative Reductive Growth and Oxidative Dissolution Reactions. *J. Am. Chem. Soc.* **2014**, *136*, 7603−7606.

(15) Lin, H. X.; Lei, Z. C.; Jiang, Z. Y.; Hou, C. P.; Liu, D. Y.; Xu, M. M.; Tian, Z. Q.; Xie, Z. X. Supersaturation-Dependent Surface Structure Evolution: From Ionic, Molecular to Metallic Micro/Nanocrystals. *J. Am. Chem. Soc.* **2013**, *135*, 9311−9314.

(16) Quan, Z. W.; Wang, Y. X.; Fang, J. Y. High-Index Faceted Noble Metal Nanocrystals. *Acc. Chem. Res.* **2013**, *46*, 191−202.

(17) Murphy, C. J.; Thompson, L. B.; Alkilany, A. M.; Sisco, P. N.; Boulos, S. P.; Sivapalan, S. T.; Yang, J. A.; Chernak, D. J.; Huang, J. Y. The Many Faces of Gold Nanorods. *J. Phys. Chem. Lett.* **2010**, *1*, 2867−2875.

(18) Lohse, S. E.; Murphy, C. J. The Quest for Shape Control: A History of Gold Nanorod Synthesis. *Chem. Mater.* **2013**, *25*, 1250−1261.

(19) Chen, H. J.; Shao, L.; Li, Q.; Wang, J. F. Gold Nanorods and Their Plasmonic Properties. *Chem. Soc. Rev.* **2013**, *42*, 2679−2724.

(20) Huang, X. H.; Neretina, S.; El-Sayed, M. A. Gold Nanorods: From Synthesis and Properties to Biological and Biomedical Applications. *Adv. Mater.* **2009**, *21*, 4880−4910.

(21) Nikoobakht, B.; El-Sayed, M. A. Preparation and Growth Mechanism of Gold Nanorods (NRs) using Seed-Mediated Growth Method. *Chem. Mater.* **2003**, *15*, 1957−1962.

(22) Millstone, J. E.; Hurst, S. J.; Metraux, G. S.; Cutler, J. I.; Mirkin, C. A. Colloidal Gold and Silver Triangular Nanoprisms. *Small* **2009**, *5*, 646−664.

(23) Chiu, C. Y.; Chung, P. J.; Lao, K. U.; Liao, C. W.; Huang, M. H. Facet-Dependent Catalytic Activity of Gold Nanocubes, Octahedra, and Rhombic Dodecahedra toward 4-Nitroaniline Reduction. *J. Phys. Chem. C* **2012**, *116*, 23757−23763.

(24) Lu, C. L.; Prasad, K. S.; Wu, H. L.; Ho, J. A. A.; Huang, M. H. Au Nanocube-Directed Fabrication of Au-Pd Core-Shell Nanocrystals with Tetrahexahedral, Concave Octahedral, and Octahedral Structures and Their Electrocatalytic Activity. *J. Am. Chem. Soc.* **2010**, *132*, 14546−14553.

(25) Ming, T.; Feng, W.; Tang, Q.; Wang, F.; Sun, L. D.; Wang, J. F.; Yan, C. H. Growth of Tetrahexahedral Gold Nanocrystals with High-index Facets. *J. Am. Chem. Soc.* **2009**, *131*, 16350−16351.

(26) Niu, W. X.; Zhang, W. Q.; Firdoz, S.; Lu, X. M. Controlled Synthesis of Palladium Concave Nanocubes with Sub-10-Nanometer Edges and Corners for Tunable Plasmonic Property. *Chem. Mater.* **2014**, *26*, 2180−2186.

(27) Personick, M. L.; Langille, M. R.; Zhang, J.; Mirkin, C. A. Shape Control of Gold Nanoparticles by Silver Underpotential Deposition. *Nano Lett.* **2011**, *11*, 3394−3398.

(28) Tao, A.; Sinsermsuksakul, P.; Yang, P. D. Polyhedral silver nanocrystals with distinct scattering signatures. *Angew. Chem., Int. Ed.* **2006**, *45*, 4597−4601.

(29) Xia, X. H.; Zeng, J.; McDearmon, B.; Zheng, Y. Q.; Li, Q. G.; Xia, Y. N. Silver Nanocrystals with Concave Surfaces and Their Optical and Surface-Enhanced Raman Scattering Properties. *Angew. Chem., Int. Ed.* **2011**, *50*, 12542−12546.

(30) Zhang, Q. F.; Wang, H. Facet-Dependent Catalytic Activities of Au Nanoparticles Enclosed by High-Index Facets. *ACS Catal.* **2014**, *4*, 4027−4033.

DOI: 10.1021/acs.chemmater.6b00389
Chem. Mater. 2016, 28, 2728−2741

(31) Zhang, J. A.; Langille, M. R.; Personick, M. L.; Zhang, K.; Li, S. Y.; Mirkin, C. A. Concave Cubic Gold Nanocrystals with High-Index Facets. *J. Am. Chem. Soc.* **2010**, *132*, 14012−14014.
(32) Personick, M. L.; Mirkin, C. A. Making Sense of the Mayhem behind Shape Control in the Synthesis of Gold Nanoparticles. *J. Am. Chem. Soc.* **2013**, *135*, 18238−18247.
(33) Ma, Y. Y.; Kuang, Q.; Jiang, Z. Y.; Xie, Z. X.; Huang, R. B.; Zheng, L. S. Synthesis of Trisoctahedral Gold Nanocrystals with Exposed High-Index Facets by a Facile Chemical Method. *Angew. Chem., Int. Ed.* **2008**, *47*, 8901−8904.
(34) Zhang, Q. F.; Large, N.; Nordlander, P.; Wang, H. Porous Au Nanoparticles with Tunable Plasmon Resonances and Intense Field Enhancements for Single-Particle SERS. *J. Phys. Chem. Lett.* **2014**, *5*, 370−374.
(35) Yu, Y.; Zhang, Q. B.; Lu, X. M.; Lee, J. Y. Seed-Mediated Synthesis of Monodisperse Concave Trisoctahedral Gold Nanocrystals with Controllable Sizes. *J. Phys. Chem. C* **2010**, *114*, 11119−11126.
(36) Liu, M. Z.; Guyot-Sionnest, P. Mechanism of Silver(I)-Assisted Growth of Gold Nanorods and Bipyramids. *J. Phys. Chem. B* **2005**, *109*, 22192−22200.
(37) Xiang, Y. J.; Wu, X. C.; Liu, D. F.; Feng, L. L.; Zhang, K.; Chu, W. G.; Zhou, W. Y.; Xie, S. S. Tuning the Morphology of Gold Nanocrystals by Switching the Growth of {110} Facets from Restriction to Preference. *J. Phys. Chem. C* **2008**, *112*, 3203−3208.
(38) Zhang, L.; Chen, Q. L.; Jiang, Z. Y.; Xie, Z. X.; Zheng, L. S. Cu^{2+} Underpotential-Deposition Assisted Synthesis of Au and Au−Pd Alloy Nanocrystals with Systematic Shape Evolution. *CrystEngComm* **2015**, *17*, 5556−5561.
(39) Zhang, L.; Zhang, J. W.; Kuang, Q.; Xie, S. F.; Jiang, Z. Y.; Xie, Z. X.; Zheng, L. S. Cu^{2+}-Assisted Synthesis of Hexoctahedral Au-Pd Alloy Nanocrystals with High-Index Facets. *J. Am. Chem. Soc.* **2011**, *133*, 17114−17117.
(40) Padmos, J. D.; Personick, M. L.; Tang, Q.; Duchesne, P. N.; Jiang, D.-E.; Mirkin, C. A.; Zhang, P. The Surface Structure of Silver-Coated Gold Nanocrystals and its Influence on Shape Control. *Nat. Commun.* **2015**, *6*, 7664.
(41) Mallin, M. P.; Murphy, C. J. Solution-Phase Synthesis of Sub-10 nm Au-Ag Alloy Nanoparticles. *Nano Lett.* **2002**, *2*, 1235−1237.
(42) DeSantis, C. J.; Weiner, R. G.; Radmilovic, A.; Bower, M. M.; Skrabalak, S. E. Seeding Bimetallic Nanostructures as a New Class of Plasmonic Colloids. *J. Phys. Chem. Lett.* **2013**, *4*, 3072−3082.
(43) Huang, J. F.; Zhu, Y. H.; Lin, M.; Wang, Q. X.; Zhao, L.; Yang, Y.; Yao, K. X.; Han, Y. Site-Specific. Growth of Au-Pd Alloy Horns on Au Nanorods: A Platform for Highly Sensitive Monitoring of Catalytic Reactions by Surface Enhancement Raman Spectroscopy. *J. Am. Chem. Soc.* **2013**, *135*, 8552−8561.
(44) DeSantis, C. J.; Peverly, A. A.; Peters, D. G.; Skrabalak, S. E. Octopods versus Concave Nanocrystals: Control of Morphology by Manipulating the Kinetics of Seeded Growth via Co-Reduction. *Nano Lett.* **2011**, *11*, 2164−2168.
(45) DeSantis, C. J.; Sue, A. C.; Bower, M. M.; Skrabalak, S. E. Seed-Mediated Co-reduction: A Versatile Route to Architecturally Controlled Bimetallic Nanostructures. *ACS Nano* **2012**, *6*, 2617−2628.
(46) Shibata, T.; Bunker, B. A.; Zhang, Z. Y.; Meisel, D.; Vardeman, C. F.; Gezelter, J. D. Size-Dependent Spontaneous Alloying of Au-Ag Nanoparticles. *J. Am. Chem. Soc.* **2002**, *124*, 11989−11996.
(47) Edgar, J. A.; McDonagh, A. M.; Cortie, M. B. Formation of Gold Nanorods by a Stochastic "Popcorn" Mechanism. *ACS Nano* **2012**, *6*, 1116−1125.
(48) Walsh, M. J.; Barrow, S. J.; Tong, W. M.; Funston, A. M.; Etheridge, J. Symmetry Breaking and Silver in Gold Nanorod Growth. *ACS Nano* **2015**, *9*, 715−724.
(49) Jackson, S. R.; McBride, J. R.; Rosenthal, S. J.; Wright, D. W. Where's the Silver? Imaging Trace Silver Coverage on the Surface of Gold Nanorods. *J. Am. Chem. Soc.* **2014**, *136*, 5261−5263.
(50) Almora-Barrios, N.; Novell-Leruth, G.; Whiting, P.; Liz-Marzan, L. M.; Lopez, N. Theoretical Description of the Role of Halides, Silver, and Surfactants on the Structure of Gold Nanorods. *Nano Lett.* **2014**, *14*, 871−875.
(51) Katz-Boon, H.; Rossouw, C. J.; Weyland, M.; Funston, A. M.; Mulvaney, P.; Etheridge, J. Three-Dimensional Morphology and Crystallography of Gold Nanorods. *Nano Lett.* **2011**, *11*, 273−278.
(52) Carbo-Argibay, E.; Rodriguez-Gonzalez, B.; Gomez-Grana, S.; Guerrero-Martinez, A.; Pastoriza-Santos, I.; Perez-Juste, J.; Liz-Marzan, L. M. The Crystalline Structure of Gold Nanorods Revisited: Evidence for Higher-Index Lateral Facets. *Angew. Chem., Int. Ed.* **2010**, *49*, 9397−9400.
(53) Goris, B.; Bals, S.; Van den Broek, W.; Carbo-Argibay, E.; Gomez-Grana, S.; Liz-Marzan, L. M.; Van Tendeloo, G. Atomic-Scale Determination of Surface Facets in Gold Nanorods. *Nat. Mater.* **2012**, *11*, 930−935.
(54) Gai, P. L.; Harmer, M. A. Surface Atomic Defect Structures and Growth of Gold Nanorods. *Nano Lett.* **2002**, *2*, 771−774.
(55) Wang, Z. L.; Gao, R. P.; Nikoobakht, B.; El-Sayed, M. A. Surface Reconstruction of the Unstable {110} Surface in Gold Nanorods. *J. Phys. Chem. B* **2000**, *104*, 5417−5420.
(56) Katz-Boon, H.; Walsh, M.; Dwyer, C.; Mulvaney, P.; Funston, A. M.; Etheridge, J. Stability of Crystal Facets in Gold Nanorods. *Nano Lett.* **2015**, *15*, 1635−41.
(57) Gou, L. F.; Murphy, C. J. Fine-Tuning the Shape of Gold Nanorods. *Chem. Mater.* **2005**, *17*, 3668−3672.
(58) Song, J. H.; Kim, F.; Kim, D.; Yang, P. D. Crystal Overgrowth on Gold Nanorods: Tuning the Shape, Facet, Aspect Ratio, and Composition of the Nanorods. *Chem. - Eur. J.* **2005**, *11*, 910−916.
(59) Kou, X. S.; Zhang, S. Z.; Yang, Z.; Tsung, C. K.; Stucky, G. D.; Sun, L. D.; Wang, J. F.; Yan, C. H. Glutathione- and Cysteine-Induced Transverse Overgrowth on Gold Nanorods. *J. Am. Chem. Soc.* **2007**, *129*, 6402−6404.
(60) Sohn, K.; Kim, F.; Pradel, K. C.; Wu, J. S.; Peng, Y.; Zhou, F. M.; Huang, J. X. Construction of Evolutionary Tree for Morphological Engineering of Nanoparticles. *ACS Nano* **2009**, *3*, 2191−2198.
(61) Khlebtsov, B. N.; Khanadeev, V. A.; Ye, J.; Sukhorukov, G. B.; Khlebtsov, N. G. Overgrowth of Gold Nanorods by Using a Binary Surfactant Mixture. *Langmuir* **2014**, *30*, 1696−1703.
(62) Liu, W. Q.; Zhang, H.; Wen, T.; Yan, J.; Hou, S.; Shi, X. W.; Hu, Z. J.; Ji, Y. L.; Wu, X. C. Activation of Oxygen-Mediating Pathway Using Copper Ions: Fine-Tuning of Growth Kinetics in Gold Nanorod Overgrowth. *Langmuir* **2014**, *30*, 12376−12383.
(63) Huang, Y. J.; Wu, L.; Chen, X. D.; Bai, P.; Kim, D. H. Synthesis of Anisotropic Concave Gold Nanocuboids with Distinctive Plasmonic Properties. *Chem. Mater.* **2013**, *25*, 2470−2475.
(64) Zhang, L. F.; Zhang, C. Y. Controlled Growth of Concave Gold Nanobars with High Surface-Enhanced Raman-Scattering and Excellent Catalytic Activities. *Nanoscale* **2013**, *5*, 5794−5800.
(65) Huang, J. F.; Zhu, Y. H.; Liu, C. X.; Zhao, Y. F.; Liu, Z. H.; Hedhili, M. N.; Fratalocchi, A.; Han, Y. Fabricating a Homogeneously Alloyed AuAg Shell on Au Nanorods to Achieve Strong, Stable, and Tunable Surface Plasmon Resonances. *Small* **2015**, *11*, 5214−5221.
(66) Bai, T. L.; Sun, J. F.; Che, R. C.; Xu, L. N.; Yin, C. Y.; Guo, Z. R.; Gu, N. Controllable Preparation of Core-Shell Au-Ag Nanoshuttles with Improved Refractive Index Sensitivity and SERS Activity. *ACS Appl. Mater. Interfaces* **2014**, *6*, 3331−3340.
(67) Vigderman, L.; Zubarev, E. R. Starfruit-Shaped Gold Nanorods and Nanowires: Synthesis and SERS Characterization. *Langmuir* **2012**, *28*, 9034−9040.
(68) Zhang, Q. F.; Zhou, Y. D.; Villarreal, E.; Lin, Y.; Zou, S. L.; Wang, H. Faceted Gold Nanorods: Nanocuboids, Convex Nanocuboids, and Concave Nanocuboids. *Nano Lett.* **2015**, *15*, 4161−4169.
(69) Zhang, Q. F.; Han, L. L.; Jing, H.; Blom, D. A.; Lin, Y.; Xin, H. L.; Wang, H. Facet Control of Gold Nanorods. *ACS Nano* **2016**, *10*, 2960−2974.
(70) Ye, X. C.; Zheng, C.; Chen, J.; Gao, Y. Z.; Murray, C. B. Using Binary Surfactant Mixtures To Simultaneously Improve the Dimensional Tunability and Monodispersity in the Seeded Growth of Gold Nanorods. *Nano Lett.* **2013**, *13*, 765−771.
(71) Park, S.; Sinha, N.; Hamad-Schifferli, K. Effective Size and Zeta Potential of Nanorods by Ferguson Analysis. *Langmuir* **2010**, *26*, 13071−13075.

DOI: 10.1021/acs.chemmater.6b00389
Chem. Mater. 2016, 28, 2728−2741

(72) Hore, M. J. A.; Ye, X. C.; Ford, J.; Gao, Y. Z.; Fei, J. Y.; Wu, Q.; Rowan, S. J.; Composto, R. J.; Murray, C. B.; Hammouda, B. Probing the Structure, Composition, and Spatial Distribution of Ligands on Gold Nanorods. *Nano Lett.* **2015**, *15*, 5730−5738.
(73) Lee, J. H.; Gibson, K. J.; Chen, G.; Weizmann, Y. Bipyramid-templated synthesis of monodisperse anisotropic gold nanocrystals. *Nat. Commun.* **2015**, *6*, 7571.
(74) DuChene, J. S.; Niu, W. X.; Abendroth, J. M.; Sun, Q.; Zhao, W. B.; Huo, F. W.; Wei, W. D. Halide Anions as Shape-Directing Agents for Obtaining High-Quality Anisotropic Gold Nanostructures. *Chem. Mater.* **2013**, *25*, 1392−1399.
(75) Millstone, J. E.; Wei, W.; Jones, M. R.; Yoo, H. J.; Mirkin, C. A. Iodide Ions Control Seed-Mediated Growth of Anisotropic Gold Nanoparticles. *Nano Lett.* **2008**, *8*, 2526−2529.
(76) Pallares, R. M.; Su, X. D.; Lim, S. H.; Thanh, N. T. K. Fine-Tuning of Gold Nanorod Dimensions and Plasmonic Properties Using the Hofmeister Effects. *J. Mater. Chem. C* **2016**, *4*, 53−61.
(77) Nishimura, S.; Dao, A. T. N.; Mott, D.; Ebitani, K.; Maenosono, S. X-Ray Absorption Near-Edge Structure and X-ray Photoelectron Spectroscopy Studies of Interfacial Charge Transfer in Gold-Silver-Gold Double-Shell Nanoparticles. *J. Phys. Chem. C* **2012**, *116*, 4511−4516.
(78) Srnova-Sloufova, I.; Vlckova, B.; Bastl, Z.; Hasslett, T. L. Bimetallic (Ag)Au Nanoparticles Prepared by the Seed Growth Method: Two-Dimensional Assembling, Characterization by Energy Dispersive X-Ray Analysis, X-Ray Photoelectron Spectroscopy, and Surface Enhanced Raman Spectroscopy, and Proposed Mechanism of Growth. *Langmuir* **2004**, *20*, 3407−3415.
(79) Vigderman, L.; Zubarev, E. R. High-Yield Synthesis of Gold Nanorods with Longitudinal SPR Peak Greater than 1200 nm Using Hydroquinone as a Reducing Agent. *Chem. Mater.* **2013**, *25*, 1450−1457.
(80) Xie, J. P.; Lee, J. Y.; Wang, D. I. C. Seedless, Surfactantless, High-Yield Synthesis of Branched Gold Nanocrystals in HEPES Buffer Solution. *Chem. Mater.* **2007**, *19*, 2823−2830.
(81) Gao, C. B.; Hu, Y. X.; Wang, M. S.; Chi, M. F.; Yin, Y. D. Fully Alloyed Ag/Au Nanospheres: Combining the Plasmonic Property of Ag with the Stability of Au. *J. Am. Chem. Soc.* **2014**, *136*, 7474−7479.
(82) Park, K.; Vaia, R. A. Synthesis of Complex Au/Ag Nanorods by Controlled Overgrowth. *Adv. Mater.* **2008**, *20*, 3882−3886.
(83) Liu, K. K.; Tadepalli, S.; Tian, L. M.; Singamaneni, S. Size-Dependent Surface Enhanced Raman Scattering Activity of Plasmonic Nanorattles. *Chem. Mater.* **2015**, *27*, 5261−5270.
(84) Xiong, W.; Sikdar, D.; Yap, L. W.; Premaratne, M.; Li, X. Y.; Cheng, W. L. Multilayered Core-Satellite Nanoassemblies with Fine-Tunable Broadband Plasmon Resonances. *Nanoscale* **2015**, *7*, 3445−3452.
(85) Jing, H.; Zhang, Q. F.; Large, N.; Yu, C. M.; Blom, D. A.; Nordlander, P.; Wang, H. Tunable Plasmonic Nanoparticles with Catalytically Active High-Index Facets. *Nano Lett.* **2014**, *14*, 3674−3682.
(86) Jiang, R. B.; Chen, H. J.; Shao, L.; Li, Q.; Wang, J. F. Unraveling the Evolution and Nature of the Plasmons in (Au Core)-(Ag Shell) Nanorods. *Adv. Mater.* **2012**, *24*, OP200−OP207.
(87) Okuno, Y.; Nishioka, K.; Kiya, A.; Nakashima, N.; Ishibashi, A.; Niidome, Y. Uniform and Controllable Preparation of Au-Ag Core-Shell Nanorods using Anisotropic Silver Shell Formation on Gold Nanorods. *Nanoscale* **2010**, *2* (8), 1489−1493.
(88) Jing, H.; Large, N.; Zhang, Q. F.; Wang, H. Epitaxial Growth of Cu_2O on Ag Allows for Fine Control Over Particle Geometries and Optical Properties of Ag-Cu_2O Core-Shell Nanoparticles. *J. Phys. Chem. C* **2014**, *118*, 19948−19963.
(89) Fang, C. H.; Lee, Y. H.; Shao, L.; Jiang, R. B.; Wang, J. F.; Xu, Q. H. Correlating the Plasmonic and Structural Evolutions during the Sulfidation of Silver Nanocubes. *ACS Nano* **2013**, *7*, 9354−9365.

DOI: 10.1021/acs.chemmater.6b00389
Chem. Mater. 2016, 28, 2728−2741